Single Iridium Atom Doped Ni_2P Catalyst for Optimal Oxygen Evolution

Qi Wang [#1], *Zhe zhang*[#2], *Chao Cai* [#1], *Maoyu Wang*[3], *Zhi Liang Zhao*[1], *Xiang Huang*[2], *Shaobo Han* [#1], *Xiaobo Shi*[1], *Zhou Hua*[5], *Zhenxing Feng*[3], *Jun Li(李隽)*[4], *Hu Xu**[2], *Meng Gu* *[1]

[1]Department of Materials Science and Engineering, Southern University of Science and Technology, Shenzhen 518055, China

[2]Department of Physics, Southern University of Science and Technology, Shenzhen 518055, China

[3]School of Chemical, Biological and Environment Engineering, Oregon State University, Oregon 97331, United States

[4]Department of Chemistry Southern University of Science and Technology, Shenzhen 518055, China

[5]X-ray Science Division, Argonne National Laboratory, Lemont, IL, 60439, United States

 # These people contribute equally to this work

Abstract

Single atom catalysts with isolated functional active atoms offer tremendous potential for many chemical reactions, including the kinetically limited oxygen evolution reaction. However, massive production of stably anchored single atoms remains a big challenge. Here we report a simple phosphating process to fabricate high-density Ir single atom catalysts on Ni_2P. Careful structural analysis indicate that Ir atoms preferentially occupies the Ni sites at the top surface and the Ir-O-P/Ni-O-P bonding environments favors optimum absorption and desorption of OER intermediate species. The specific structure endows the Ir_{SA}-Ni_2P catalyst a record low overpotential of ~149 mV at the

current density of 10 mA·cm^{-2} in 1.0 M KOH, which is ~28 folds of the commercial IrO_2 efficiency. In addition, transmission electron microscopy (TEM) and X-ray photoelectron spectroscopy (XPS) study directly revealed the transformation of Ni@Ir particles to Ir_{SA}-Ni_2P hollow spheres. The exceptional "top-down" strategy provides a brand new approach to fabricate single atom catalysts for useful chemical reactions and energy conversion.

Introduction

Electrochemical water splitting is regarded as one of the most promising pathways for producing hydrogen, which converts the sustainable-renewable energy into useful chemical energy. [1]However, the hydrogen production efficiency is severely constrained by the sluggish kinetics of the oxygen evolution reaction (OER).[2] To realize the industrial applications of electrolytic water splitting systems, catalysts with low overpotential, high mass activity, and high durability must be found to reduce the energy cost.[3] Currently, precious metal oxide, such as IrO_2 and RuO_2 represents the benchmark OER activity.[4] These precious metal catalysts are costly, scarce, and often short-living, which seriously hinders their industrial-scale applications.[5] After decades' effort, the state-of-the-art OER catalysts are reported to deliver an overpotential of around 200 mV at the current density of 10 cm·cm^{-2} in alkaline. Further reducing the reaction overpotential and enhancing the activity of OER catalysts remain challenging.

Single-atom catalyst (SAC) with atomically dispersed active metal atoms stably anchored on a support is considered as one of the most promising strategy to minimize the usage of precious metals without compromising the catalytic performance.[6-7] In addition, further enhancement of the activity and selectivity can be reached by careful tuning of the electronic structure between the doped single atom and surrounding support atoms.[6, 8-9] Nowadays, various strategies have been developed to construct atomically distributed atoms including wet-chemistry method, atomic layer deposition(ALD), ball milling strategy, galvanic replacement method, and high-temperature pyrolysis.[10-11] Nevertheless, most reported methods are based on a “bottom-up” strategy,[12] which refers to obtaining the single atom catalysts from mononuclear or multinuclear metal precursors. However, isolated active atoms obtained through this route tend to migrate and aggregate during the preparation or application processes. In contrast, the “top-down” method can convert nanoparticles into well-dispersed single atom catalysts, which is simple and feasible in industrial applications. Most notably, SACs prepared with this top-down approach retains high thermodynamic stability and long-life in usage as well. A few factors governing the conversion process, such as high temperature, reaction time, migration of atoms, and precursor nanoparticles, need extensive research and tuning to successful application of top-down approach.[13] In addition, the activity and stability of single atoms are also very important aspects, which can be tuned by adjusting the local coordination environment, such as ligand atoms, support, and structural distortion.[14-15] It remains vitally challenging to provide in-depth insights into the formation mechanism of single atom and synthesize SACs at large scale.

Here, we report the successful fabrication of Ir single atom catalysts on Ni_xP_y spheres through a simple top-down phosphating process. Elevated temperatures activate the diffusion of atoms, formation of Ni_xP_y, and debonding of the Ir-metal shell into well-dispersed single Ir atoms on Ni_xP_y. The atomic and electronic structural features of different phosphating stages were tracked by transmission electron microscopy (TEM) and x-ray photoelectron spectroscopy (XPS) to further elucidate the formation mechanism of single atom catalysts. Furthermore, we extended the synthetic route to achieve other single atoms decorated Ni_2P including Ru, Rh and Au. Together, our findings provide a general “top-down” synthetic strategy for developing highly efficient single atom decorated metal phosphide catalysts.

Results and Discuss

Catalyst synthesis and characterization

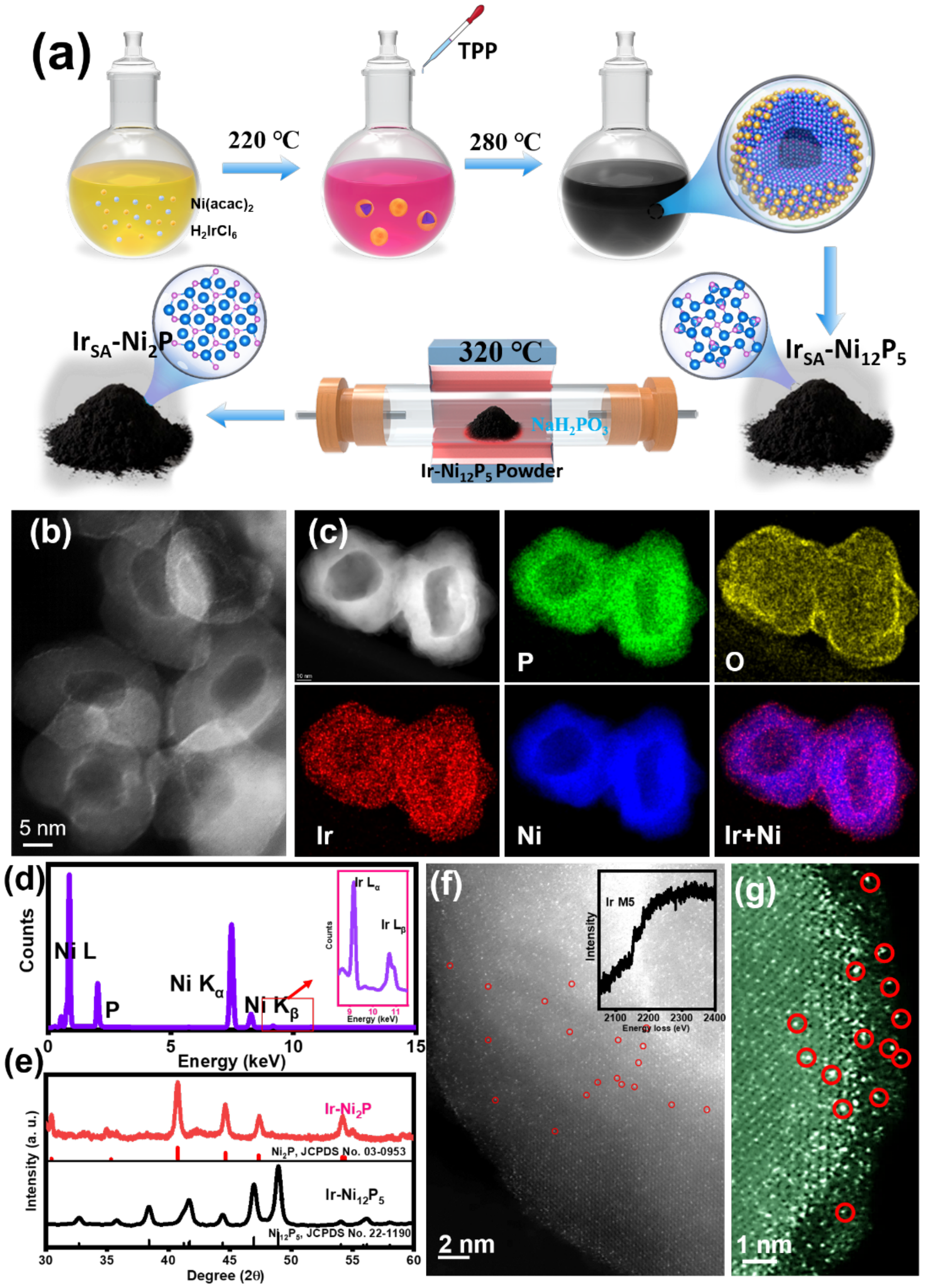

Figure 1. (a) Schematic illustration of the synthetic procedure. (b) corresponding STEM images of typical Ir_{SA}-Ni_2P catalyst. (c) HAADF-STEM image and EDS elemental mapping images. (d) corresponding EDS spectrum and magnified spectrum of Ir-L characterised peaks (inserted), indicating the existance of Ir. (e) The XRD

patterns of Ir_{SA}-Ni_2P and Ir_{SA}-$Ni_{12}P_5$. (f-g) High-resolution HAADF-STEM image of Ir-SAs, suggesting Ir was atomically dispersed on the Ni_2P substrate, the EELS Ir-M edge of brighter spots was inserted.

To obtain the catalyst, certain amounts of nickel acetylacetone and Chloroiridium acid were dissolved into 10 mL OAm and 10 mL ODE at 120^0C. The mixed solution was heated to 220^0C and stored for 1 hour to aid the formation of Ir-Ni particle. Then triphenylphosphine (TPP) was added into the solution and heated to 280 ^{0}C to initiate the phosphating process. A heating process was followed to convert the $Ni_{12}P_5$ to Ni_2P, as illustrated in Figure 1a. Aberration-corrected high-angle annular dark-field scanning transmission electron microscopy (HAADF-STEM) was firstly carried out to analyze the morphology, element distribution and location of Nickle Phosphides-based catalyst. The low-magnification STEM image of final products was displayed in Figure 1b that reveals the nanoparticle as hollow nanospheres with a diameter of 20-60 nm. The EDS-mapping in Figure 1c presents the elemental distribution of Ir, Ni and P, which suggests that all elements are evenly distributed. The atomic ratio of Ir, Ni is 1:66 as determined by EDS spectrum analysis (Figure 1d). The heavy Ir atoms manifest higher contrast than nickle in such Z-contrast imaging mode. Atomic scale STEM analysis of iridium atoms in Figure 1 f-g clearly shows that iridium atoms were well dispersed on the Ni_2P nanospheres. Detailed look at the edge of sphere (Figure 1g) reveals an amorphous $Ni(P_yO_x)$ layer decorated with isolated iridium atoms (Figure S2). The density of iridium atoms at the edges or surfaces seems to be quite high as shown by STEM imaging in Figure 1g and EDS element line-profile (Figure S2c). The EELS in Figure 1g further confirmed the identity of these bright atoms to be Ir single atoms. The crystal structure of Ir_{SA}-Ni_2P was further verified by Xray diffraction (XRD) (Figure 1e). The analysis of patterns verified the emergence of a crystalline Ni_2P with no other phases. Compared with standard Ni_2P (JCPDS No. 03-0953) and $Ni_{12}P_5$ (JCPDS No. 22-1190) or prepared Ni_2P and $Ni_{12}P_5$ XRD patterns (Figure S1), the Ir single atom doped Ni_2P and $Ni_{12}P_5$ show same peak positions, indicating similar lattice constants between Ir single atom doped/undoped Ni_2P and $Ni_{12}P_5$. Couple with the EDS, it is believed that most Ir atoms are resided on the surface of Ni_2P or $Ni_{12}P_5$ other than incorporated in the lattice.

Atomic and electronic structure recognition

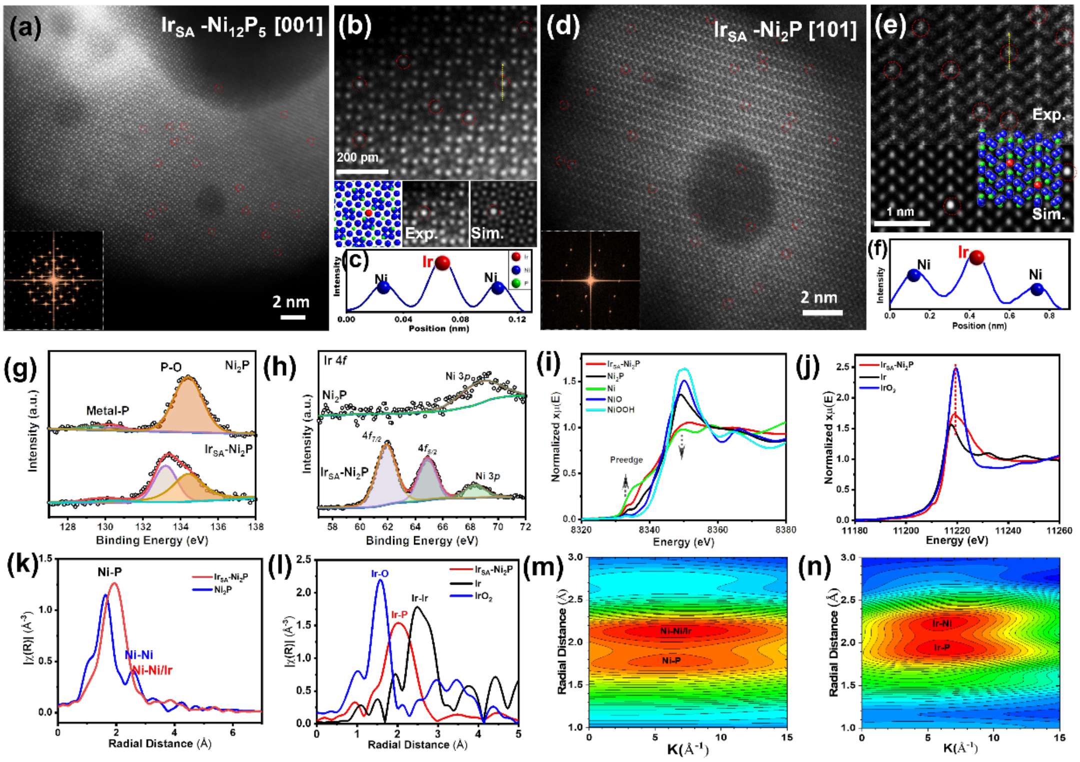

Figure 2. (a) Atomic-resolution HAADF-STEM image and corresponding FFT (inserted) of Ir_{SA}-$Ni_{12}P_5$, projected along [001] zone axis of $Ni_{12}P_5$. (b) Atomic model, experimental and simulated HAADF-STEM images of Ir_{SA}-$Ni_{12}P_5$ (c) Intensity profile of the yellow line in the (b), with the matrix Ni column and the decorated Ir atom marked according to the HAADF intensity variation. (d) Atomic-resolution HAADF-STEM image and corresponding FFT (inserted) of Ir_{SA}-Ni_2P, projected along [101] zone axis of Ir_{SA}-Ni_2P. (e) Atomic model, experimental and simulated HAADF-STEM images of Ir_{SA}-Ni_2P (f) Intensity profile of the yellow line in the (e), with the matrix Ni column and the decorated Ir atom marked according to the HAADF intensity variation. (g) High-resolution XPS spectra of Ir_{SA}-Ni_2P and Ni_2P for P 2p and (h) Ir 4f. (i) The Ni K-edge and (j) Ir L-edge XANES spectra of Ir_{SA}-Ni_2P. Fourier-transformed EXAFS spectra at (k) Ni K-edge and (l) Ir L-edge of Ir_{SA}-Ni_2P catalyst and the references. the corresponding wavelet transforms for the Ni K-edge (m) and Ir

L3−edge EXAFS (n) signals of Ir_{SA}-Ni_2P.

Furthermore, detailed structure of isolated iridium atom position on phosphating nickel were carefully studied by atomic HAADF-STEM images. Figure 2a shows the HAADF-STEM image of Ir_{SA}-$Ni_{12}P_5$ particles view along [001] zone axis. Iridium atoms were found to evenly and separately embedded in the lattice of $Ni_{12}P_5$ revealed by brighter spots of Z-contrast images (Figure 2c). The comparison between simulated and experimental images in Fig. 3b confirms that the iridium atoms reside only in the surface Ni position of $Ni_{12}P_5$ crystal. The EDS-mapping in Figure S4a further confirmed the uniform dispersed iridium atoms. The HAADF-STEM image of Ir_{SA}-Ni_2P particles view along [101] zone axis in Figure 2d-f reveals isolated iridium atoms with higher brightness. These Ir atoms were uniformly dispersed in the position of Ni atoms (labeled by red circle) in Figure 2d-f. The atomic model, experimental images and simulated images matched each other well, indicating the reliability of iridium location at the Ni sites. The atomic EDS-mapping of Ir_{SA}-Ni_2P substantiated the highly dispersed feature of Ir in Ni_2P consistent with the HAADF-images. In sum, both the Ir-$Ni_{12}P_5$ and Ir-Ni_2P nanospheres show that iridium replaces the nickel sites.

Since the coordination environment would severely determine the electronic structure, we explored the valance state of both Ir, Ni and P via X-ray photoelectron spectroscopy (XPS). The high-resolution XPS spectrum of P 2*p* in Figure 2g reveals the presence of Ni-P bond at 129.6 eV and 130.5 and Ni-O-P bond at 134.4 eV for pure Ni_2P.[16] However, negligible signals of phosphides were detected on the surface of Ir_{SA}-Ni_2P. In addition to the Ni-O-P bond at 134.4 eV, a peak at 133.1 eV can also be detected, which could be attributed to Ir-O-P bond. In the high-resolution XPS spectra of Ir 4*f* region, notable features of iridium species with characteristic peaks at 61.9 and 64.9 eV were found, which can be attributed to Ir^{4+}.[17] The peak at around 68 eV can be attributed to Ni 3p. For the Ni 2p region, an obvious Ni-P characteristic peak at 851.9 eV can be detected Ni_2P, whereas the peak disappears in Ir_{SA}-Ni_2P samples, which is in good agreement with P 2p spectrum (Figure S8a). The result reveals that after Ir atoms were introduced on the surface of Ni_2P, the surface Ni-P bonds are more likely to convert to Metal-O-P bond. The metal phosphates are supposed to be practical and preferable interface for OER process.[18]

To further probe the local coordination environment of Ir_{SA}-Ni_2P catalyst, X-ray absorption spectroscopy (XAS) was carried out. The K-edge Ni X-ray absorption near-edge structure (XANES) position of the pre-edge peak and white line peak for both Ir_{SA}-Ni_2P and Ni_2P are about at ~8333 and ~8350 eV, respectively (Figure 2i). The white line peak decreases in intensity with Ir atoms introduction, indicating the decreased Ni valance than pure Ni_2P.[19] Meanwhile the pre-edge peak intensity increased could be related to a distortion of the octahedral coordination due to the incorporation of Ir.[20] For the Ir L-edge XANES spectra, the absorption position of Ir_{SA}-Ni_2P were close to that of IrO_2, implying the similar oxidation state, which is the same trend from XPS. (Figure 2j). To clarify the change of local coordination geometry of Ni and Ir, the curve fitting of the Fourier transforms of the extended X-ray absorption fine structure (EXAFS) for Ir_{SA}-Ni_2P was performed (Figure 2k-i, S10-11 and Table S1-2). Ir_{SA}-Ni_2P has one broad peak at around 1.9Å (Figure 2k), which could be separate into two different bonds (Ni-P at 2.1Å and Ni-Ir/Ni 2.5Å) (Table S1). Comparing with standard Ni_2P, the peak Ir introduction will extend the Ni-P bonding length, which implies the strong change of Ni geometer. The wavelet transforms (WT) signal show two intensity maxima at around 1.8Å and 2.1Å (Figure 2m), which are respectively associated with the Ni-P and Ni-Ni/Ir paths, consistent with the Ni K-edge FT-EXAFS results. The FT $k^2\ \chi(k)$ of Ir foil displays peak at around 2.5 Å, corresponding to Ir-Ir interaction which does not appear in Ir_{SA}-Ni_2P, confirming the absence of Ir nanoparticles, in line with the STEM observation. The peak of Ir_{SA}-Ni_2P at ~2.25 Å is attributed to the scattering interaction between Ir and the first shell P (Ir-P). The wavelet transform plot for Ir_{SA}-Ni_2P shows two wavelet transform plot maximal centers at around 2.0Å and 2.2Å related to Ir-P and Ir-Ni bonding, which consist with FT Ir EXAFS fitting results. (Figure 2n).

Oxygen evolution performance

Figure 3. (a) OER polarization curves of Ni_2P, $Ni_{12}P_5$, Ir_{SA}-Ni_2P, Ir_{SA}- $Ni_{12}P_5$ and commercial IrO_2. (b) Histogram of current density at 1.53 V vs. RHE. (c) the corresponding Tafel plots of (a). (d) Time-dependent current density curves of Ir_{SA}-

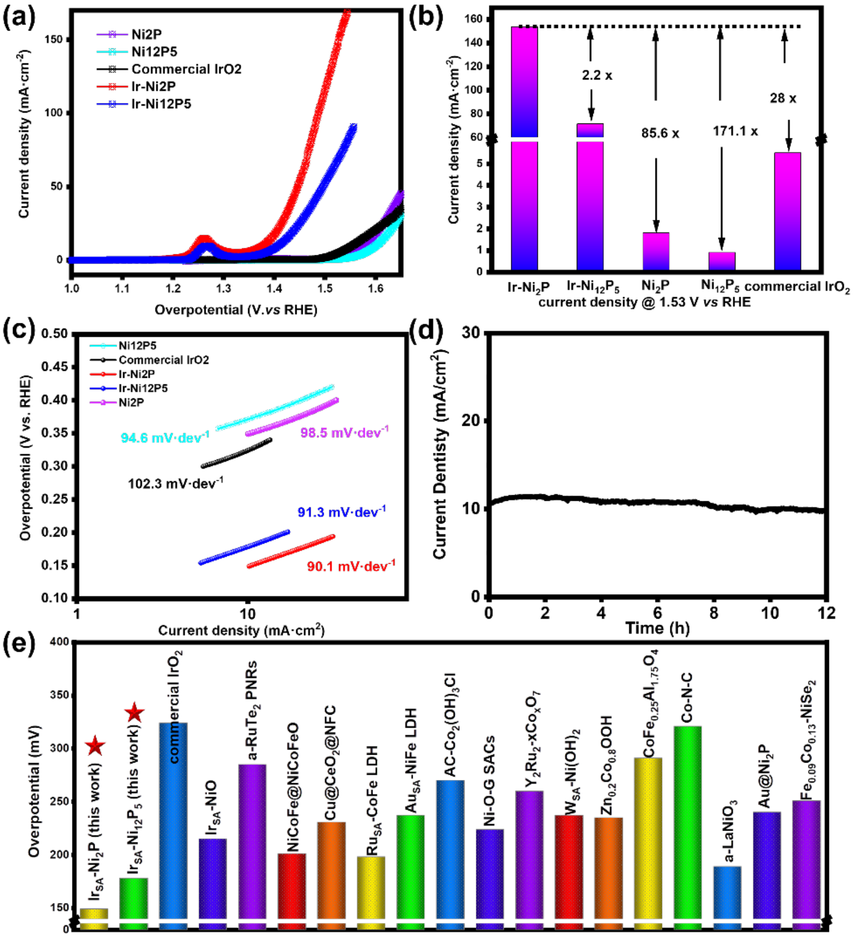

Ni_2P. (e) Comparison of the overpotential of Ir_{SA}-Ni_2P, Ir_{SA}- $Ni_{12}P_5$ and recently reported OER electrocatalysts at 10 mA cm^{-2} in 1.0 M KOH.

The OER activities of Ni_2P, $Ni_{12}P_5$, Ir_{SA}-$Ni_{12}P_5$ and Ir_{SA}-Ni_2P were evaluated and compared to commercial IrO_2. The tested samples were loaded in glass carbon (GC) as the working electrode via a typical three-electrode cell at room temperature and evaluated in N_2-saturated 1.0m KOH solutions. The linear sweep voltammetry (LSV) curves employed to evaluate the activity of these samples were show in Figure 3a with a scan rate of 5 mV·s^{-1}. It is evident that with an additional ~3 wt.% of Ir atoms, the Ir_{SA}-$Ni_{12}P_5$ and Ir_{SA}-Ni_2P show considerably enhanced OER activities than their unmodified counterparts. In particular, the Ir_{SA}-Ni_2P exhibited an outstanding overpotential of 149 mV at 10 mA·cm^{-2}, which surpassed most reported OER catalyst in alkaline electrolyte (Figure 3e). Similarly, an overpotential of 178 mV is also obtained for Ir_{SA}-$Ni_{12}P_5$. In comparison, the overpotentials of Ni_2P, $Ni_{12}P_5$ and commercial IrO_2 under same condition are 349 mV, 371 mV and 324 mV, respectively. The Tafel plots derived from the LSV polarization curves in Figure 3b reveals that the Ir_{SA}-N_2iP and Ir_{SA}-$Ni_{12}P_5$ show preeminent Tafel slope of 90.1 $mV·dec^{-1}$ and 91.3 $mV·dec^{-1}$compared with Ni_2P (98.5 $mV·dec^{-1}$), $Ni_{12}P_5$ (94.6 $mV·dec^{-1}$) and commercial IrO_2 (102.3 $mV·dec^{-1}$). Consequently, the excellent onset potential and Tafel slope of Ir_{SA}-Ni_2P is capable of delivering a current density of 154 $mA·cm^{-2}$ at overpotentials of 300 mV, which is almost 2.2 fold of Ir_{SA}-$Ni_{12}P_5$ (71.4 $mA·cm^{-2}$), 85.6 fold of Ni_2P (1.8 $mA·cm^{-2}$), 171.1 fold of $Ni_{12}P_5$ (0.9 $mA·cm^{-2}$) and 28 fold of commercial IrO_2 (5.5 $mA·cm^{-2}$), respectively (Figure 3c).

The long-term stability of Ir_{SA}-Ni_2P was measured by chronoamperometry curve at a potential of 1.38 (V vs. RHE) in Figure 3d. The sample exhibited a stable current density during the 12 h test, demonstrating stable and excellent electrochemical performance of the Ir_{SA}-Ni_2P catalyst. The structural investigation of Ir_{SA}-Ni_2P after the duration test was carried out at the atomic scale to understand their performance stability (Figure S3). According the HAADF-STEM images (Figure S3a) and EDS-mapping (Figure S3c), no structural collapse or particle aggregation was found. The hollow structure and single Ir atoms features were perfectly maintained after the harsh electrochemical cycling (Figure S3b). Therefore, the Ir_{SA}-Ni_2P not only shows extraordinary catalytic activity, but also excellent electrochemical stability, which made it a preeminent candidate for practical OER catalyst in industrial scale.

DFT Calculations

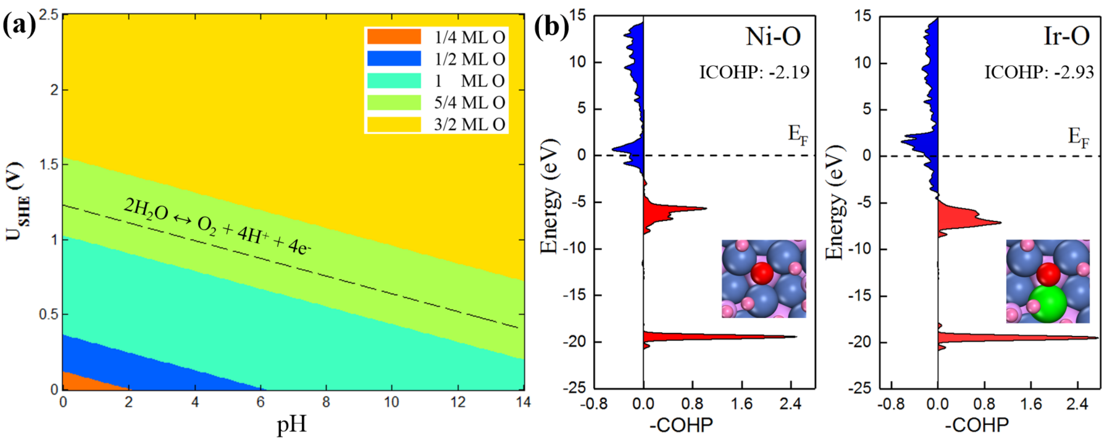

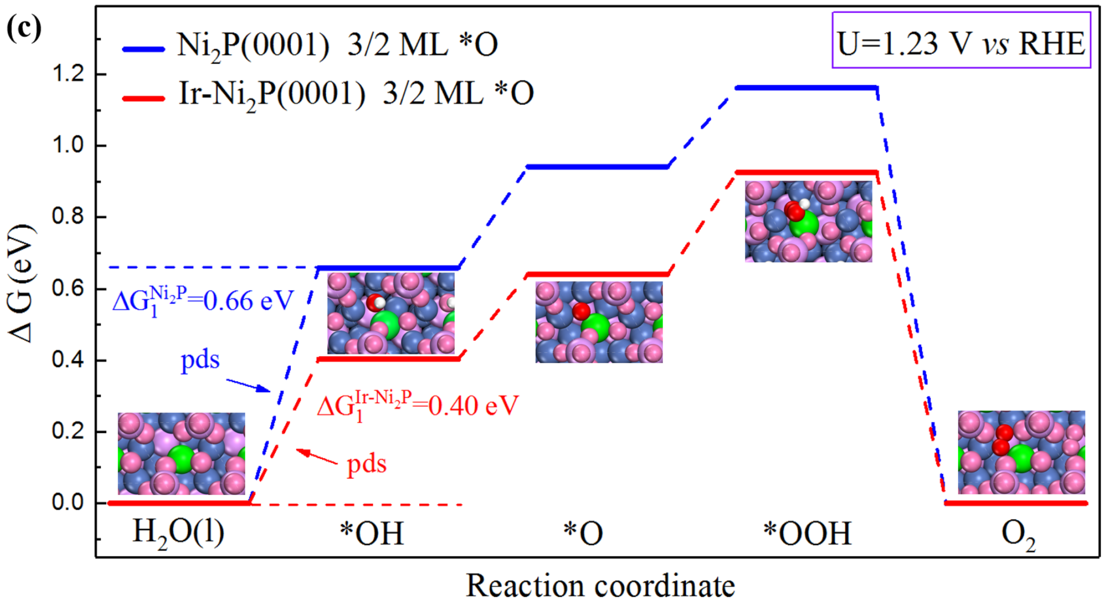

Figure 4. (a) Surface Pourbaix diagram of a single Ir atom doped Ni_2P (0001) surface (Ir@Ni_2P(0001)). (b) Projected crystal orbital Hamilton populations (COHP) between chemisorbed *O and active metal centers on Ni_2P (0001) and Ir@Ni_2P (0001). These two surfaces are both covered by 3/2 ML *O. Red and blue regions stand for bonding and antibonding contributions, respectively. (d) Free energy diagrams of OER on Ni_2P (0001) and Ir@Ni_2P (0001). Insets show the optimized OER intermediates on Ir@Ni_2P (0001). The spheres in blue, purple, green, white and pink (red) denote the Ni, P, Ir, H, and O (reaction site) atoms, respectively.

To gain insight into the excellent OER performance of Ir doped Ni_2P, we investigate the OER activity of the stable Ni_2P (0001) surface[21-22] before and after Ir atoms anchoring using computational standard hydrogen electrode (SHE) model coupled with self-consistent theoretical overpotential method.[23-24] Considering the harsh conditions of OER, we first construct the surface Pourbaix diagrams of Ni_2P(0001) and Ir@Ni_2P(0001), which are composed of the most stable surface phases at given electrode potentials and pH values (Figure S12 and S14). It is based on a balance achieved between Ni_2P(0001) (Ir@Ni_2P(0001)) and water, proton and electrons via the equations

$$* + H_2O \rightarrow *OH + H^+ + e^- \qquad (1)$$

$$*OH \rightarrow *O + H^+ + e^- \qquad (2)$$

where asterisk (*) is the active site of catalyst. Our DFT results reveal that the phosphorus, Ir and Ni atoms exposed on these two surfaces are chemically active towards H_2O, leading to the surface readily oxidized at OER operating conditions as shown in Figure 4a and S14. Specifically, for Ir@Ni_2P(0001) the surface is chemisorbed by 5/4 monolayer (ML) *O at the potential U=1.02~1.55 V *vs* RHE; promoting potential will further oxidize the surface to reach a 3/2 ML of *O, as shown in Figure 4a. Similar cases are also observed on $Ni_2P(0001)$ (Figure S12). This is in line with our experimental observation showing that an oxide layer is generated on the sample after reaction.

We next explore the oxygen evolution reaction on 5/4 and 3/2 ML *O-covered Ni_2P (0001) and Ir@Ni_2P (0001) surfaces, respectively. Figure 4c provides the self-consistent reaction scenario which means the OER can proceed on the specified surface under the potential at which that surface is stable. It is found that Ni_2P (0001) and Ir@Ni_2P (0001) both covered by 3/2 ML *O are the active surfaces for OER (Figure S13 and S15). The calculated overpotential on Ni_2P (0001) is 0.66 V with the adsorption of *OH being potential limiting step (pds). This is due to the weak binding of Ni-O on the oxidized Ni_2P (0001) surface. However, doping Ir significantly promotes the chemisorption of OER intermediates on Ni_2P (0001), as evidenced by the enhanced binding energies of *OH, *O, *OOH, which are strengthened by 0.26, 0.30 and 0.23 eV, respectively, as compared to those on $Ni_2P(0001)$ (Figure 4c). This is further verified by crystal orbital Hamilton population (COHP), which analyzes the interaction between *O intermediate and active metal centers, i.e., Ni on Ni_2P (0001) and Ir on Ir@$Ni_2P(0001)$, as shown in Figure 4b. The integrated COHP (ICOHP), which reflects the bonding contribution quantitatively, increases from -2.19 eV (Ni-*O bond) to -2.93 eV (Ir-*O bond), revealing that bonding strengthen of Ir-*O is greater than Ni-*O. As a consequence, the adsorption of *OH becomes facile on Ir@$Ni_2P(0001)$ with the overpotential reduced to 0.40 V, which surpasses commercial IrO_2 (overpotential of 0.52 V, Figure S16), showing that Ir dopant plays a critical role in promoting OER activity of Ni_2P.

Structural evolution of catalyst

Figure 5. (a) HAADF-STEM and EDX maps of original Ni@Ir core-shell nanoparticles and (b) corresponding atomic HAADF-STEM image. (c) STEM and EDX maps of samples after phosphating at 220 °C for 2 hours. (d) corresponding atomic HAADF-STEM image. (e) STEM and EDX maps of samples after phosphating at 270 °C for 2 hours. (f) corresponding atomic HAADF-STEM image.

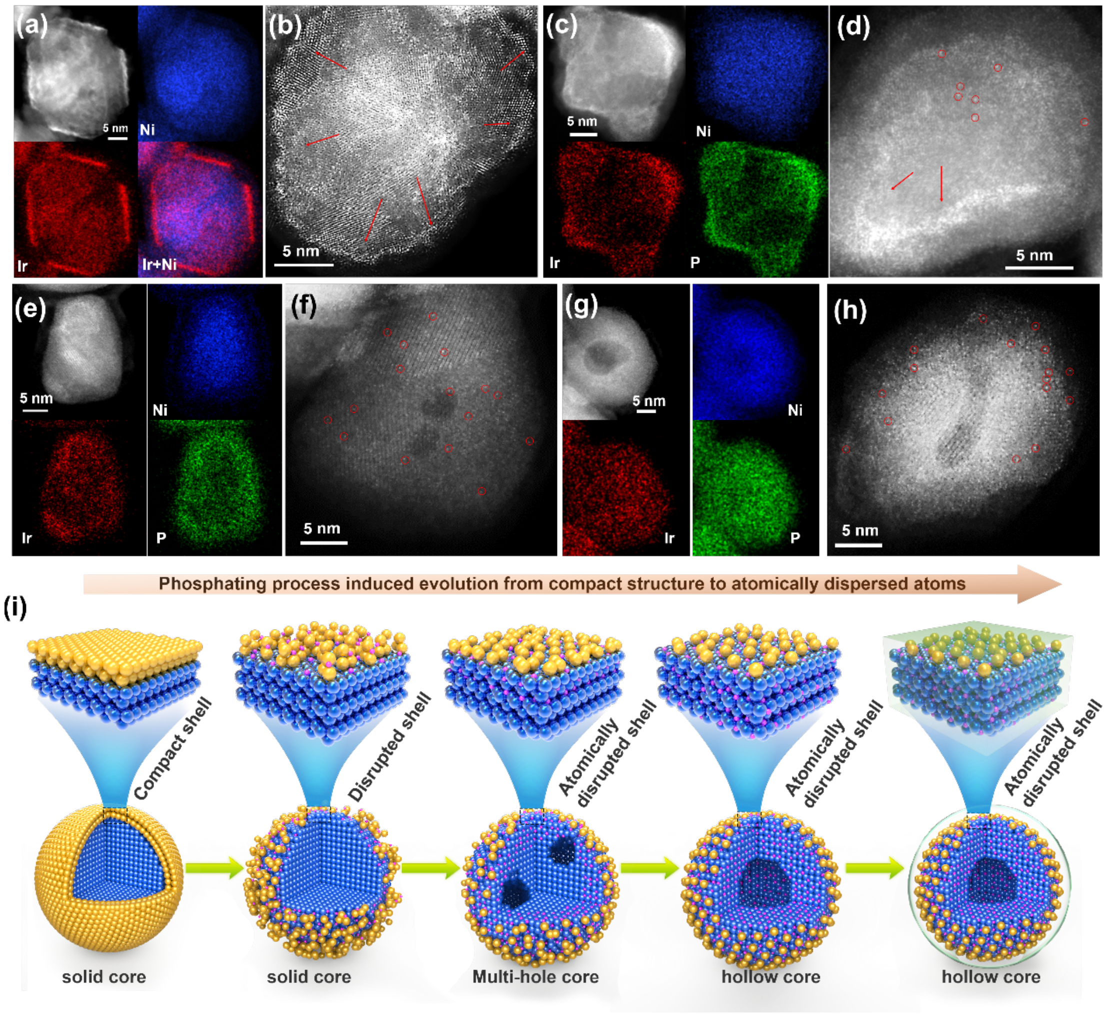

(g) STEM and EDX maps of samples after phosphating at 320 °C for 2 hours. (h) corresponding atomic HAADF-STEM image. (i) Schematic showing the evolution of nanoparticles to single atoms.

The above finding suggests that the major contributing factor of enhanced catalytic efficiency is to obtain Ni-sites occupied iridium single atoms. To get further insight of the process, we tracked the process by studying the structure changes at different degrees of phosphating process. By phosphating the Ni@Ir with different temperatures (220°C , 270°C and 320 °C) for 1 hours, the evolution during this process can be revealed. Initially, we study the structure of Ni@Ir particle before phosphating. Figure 5a presents a typical STEM images and EDS mapping at the initial Ni@Ir stage, which is a core-shell structure with iridium-shell and nickle-core. From the atomic imaging in Figure 5b, the brighter shell layer holds a d-spacing of about 2.34 Å that is attributed to (111) facet of pure iridium metal; whereas the relatively dark core region has a d-spacing of about 2.01 Å that is (111) facets of

Nickle metal. The core-shell structure maintains well after phosphating at 220 °C for 1 hour, where some P was incorporated into the shell (Figure 5c). Although the atomic STEM image in Figure 5d reveals that most iridium atoms still segregate, their periodic atomic arrangement disappeared. With increasing temperature, more P was introduced into the particles. The particles retain the morphology of solid spheres at 270 °C (Figure 5e). At this stage, the initial Ir-shell became evenly distributed Ir atoms on the surfaces (Figure 5f). The iridium atom disbandment process was occurred before the phosphating process of nickle.[25] After phosphating at 320 °C for 1 hour, the solid spheres transformed into hollow spheres with evenly distributed iridium atoms as shown in Figure 5e. During phosphating process of nickle, Kirkendall diffusion takes place to result in the final nanosphere shape. Figure S5 presents the HAADF-STEM images of structure at different phosphating degrees showing the disrupted of iridium shell. An in-situ STEM study was carried out to study the role of P during the structural evolution as well. Figure S6a displays the structure evolution of Ir-NiP-220 sample under vacuum condition. It is obviously without continuously P incorporated, the disrupted Ir atoms reassemble again (Figure S6b-c). In view of the above evidence, the overall transformation undergoes an initial iridium disbandment and following Kirkendall process (Figure 5i).

An ex-situ XPS study of surface composition and valance evolution was carried out to trace the phosphating reaction (Figure 6a). The two characteristic peaks of Ir 4f shift from 61.3 and 64.2 to 61.0 and 64 after phosphating at 220 or 270 °C for 1 hour, indicating the decrease valance after P incorporated at an initial phosphating stage. However, when reaction processed, the two peaks shifted to 61.7 eV and 64.7 eV, which is close to the Ir 4f peaks of Ir_{SA}-Ni_2P. The positive shift of the binding energies at higher temperature demonstrates the formation of Ir-O-P. Notably, after treated at 320 °C, the intensity of Ir 4f peaks suppress the Ni 3p peak, indicating a higher Ir contents after surface composition rearrangement. In the P 2p region, the Metal-P peaks also decreased with the higher phosphating degree, which is also confirmed by Ni-P bonds at Ni 2p region (Figure S9). Moreover, the Ir-O-P peaks at around 133.2 dominates the phosphate species.

To extend the scope of our synthetic strategy, we prepared three more single atom catalysts, including Ru, Rh and Au. The STEM images in Figure 6 b-d clearly demonstrate the successful preparation of well-dispersed Ru, Rh and Au single atom catalysts, respectively. The Ru sample was also analyzed using temperature-dependent approach and shown to follow the same evolution process as Ir single atom catalyst (Figure S7a-b). The general applicability of this top-down strategy gives us hope to largely scale up the fabrication of single atom catalysts for useful chemical reactions.

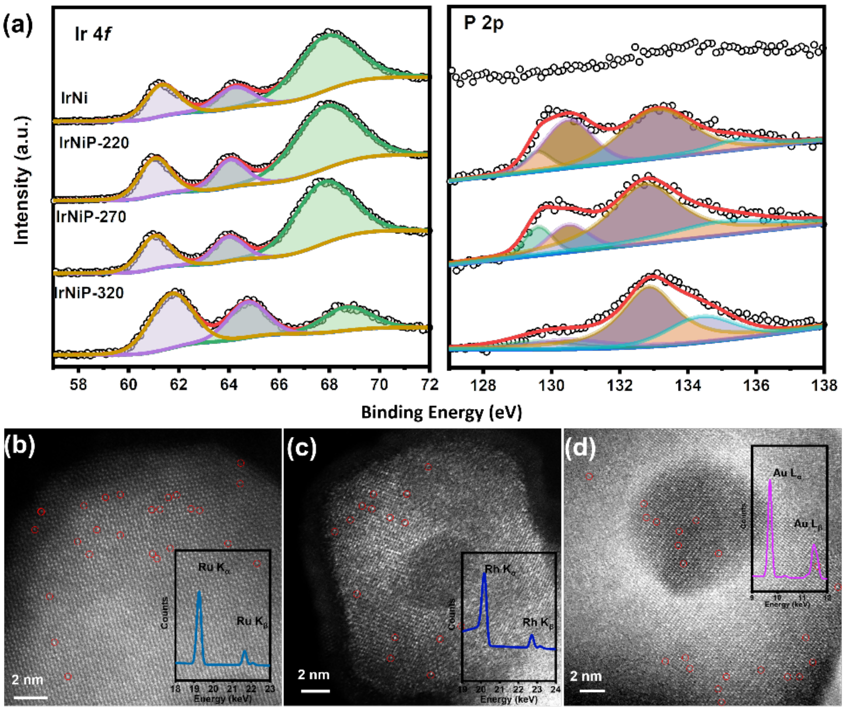

Figure 6. (a) ex-situ high-resolution XPS spectra of phosphating progress for Ir 4f and P 2p. (b-d) HAADF-STEM images of (b) Ru, (c) Rh and (d) Au single atoms doped Ni_2P, inserted were corresponding EDS spectrum indicating the existence of specific atoms.

Conclusion

We demonstrated a simple top-down phosphating strategy for scalable synthesis of single atom catalysts. The STEM and XPS shows that the evolution from nanoparticle to single atom catalysts on hollow matrix is driven by kirkendall effect. The Ir_{SA}-Ni_2P containing ~3wt% Ir exhibit a record low overpotential of 149 mV and 28 folds efficiency compared to commercial IrO_2. The fabrication route is proven to be able to fabricate multiple other single atom catalysts including Au, Ru, Rh at a large scale. This work provides new pathways for fabricating atomically dispersed single atom catalysts for practical industrial use.

Experiment

Chemicals

Oleylamie (>95%), Ammonia borane (>90%), octadecylene (>98%), Chloroiridium acid (50% metal base), nickel acetylacetone (> 95%), triphenylphosphine (>98 %), hexane (>97%), ethanol (>99%), IrO_2 (>99.9%), potassium hydroxide (99.999 %), sulfuric acid (98%) and isopropanol (99%) were purchased from alddin. Nafion solution (4.5 wt. %) was purchased from sigma.

Synthesis of Ni_2P nanoparticles

In Schlenk tube, 2 mmol nickel acetylacetone was dissolved into 10 mL OAm and 10 mL ODE at 120°C in Ar-filled glove box. The prepared transparent solution was heated to 220°C and kept at this temperature for 1 hour. 8 mmol triphenylphosphine (TPP) was added into the solution and the solution was kept at 320°C for 2 hrs before cooling down to room temperature. The black powder was collected and washed several times by hexane and ethanol at 10000 rpm for 5 min. The precipitation was redispersed in ethanol and dry in air at 60 °C for 12 hrs.

Synthesis of Ir-$Ni_{12}P_5$ nanoparticles

2 mmol nickel acetylacetone and amount of Chloroiridium acid (5 mg, 10 mg, 20 mg, 40 mg) were dissolved into 10 mL OAm and 10 mL ODE at 120^0C in Ar-filled glove box. The prepared transparent solution was heated to 220°C and kept at this temperature for 1 hour. 8 mmol triphenylphosphine (TPP) was added into the solution and the solution was kept at 280 ^0C for 2 hrs before cooling down to room temperature. The precipitation was washed and collected in a way same to Ni_2P.

Synthesis of Ir-Ni_2P nanoparticles

20 mg Ir-$Ni_{12}P_5$ and 0.4 g NaH_2PO_3 were mixed in a porcelain ark. The porcelain ark was put in a tube furnace that is full of flowing Ar. In a heating rate of 5^0C /min, the tube furnace was heated to 300 ^{0}C and held for 2 hrs. After cooling down to room temperature, the black powders were dried in air at 60 ^{0}C for 12 hrs.

Heat treatment

20 mg of as-prepared Ir@Ni_2P powder was put into a tube furnace under Ar flow at atmospheric pressure. Then the powder was heated to 350 ^{0}C for 1 hour, respectively.

Electrochemical characterization

The as-prepared samples were loaded on carbon (EC 300) with mass percentage of 20_{wt}%. Isopropanol, water and Nafion solution (with volume ratio of 1:3:0.01) was used as solution for preparing the catalyst ink (2 mg of catalyst/mL). The ink was deposited on a polished glassy carbon electrode surface as the working electrode with catalyst loading of 0.013 mg/cm^2. In a three-electrode system, 1.0 M KOH was used as electrolyte, Ag/AgCl and carbon rod was used as reference electrode and counter electrode, respectively. Before test, the working electrode was immersed into the electrolyte for 2 hrs. Line scan voltammetry (0.005 V/s) was used to characterize the catalytic performance.

Structural and chemical analysis

Bruker D8 X-ray diffractometer with Cu Kα radiation was utilized to probe the crystal structure. XPS measurements were conducted on the Axis Ultra DLD multitechnique surface analysis system and relative curves were calculated by C1s (284.8 eV). The aberration corrected STEM were performed using a double Cs-aberration corrected Themis G2 microscope at 300kV. The EDS mapping was acquired using a super-X EDS detector. XAS was performed at beamline 20-BM-D, Advanced Photon Source (APS) of Argonne National Laboratory (ANL). The ion chambers were used to collect Ir L-edge and Ni K-edge transmission signal. . Data reduction, data analysis, and EXAFS fitting were performed with the Athena, Artemis, and IFEFFIT software packages. Standard procedures were used to extract the EXAFS data from the measured absorption spectra.

Acknowledgements

This work was supported by the xxx. This work was supported by the Pico Center at SUSTech that receives support from Presidential fund and Development and Reform Commission of Shenzhen Municipality. The XAS measurements were done at beamline 20-BM-D of the Advanced Photon Source, which is a U.S. Department of Energy (DOE) Office of Science User Facility operated for the DOE Office of Science by Argonne National Laboratory under Contract No. DE-AC02-06CH11357.

Reference

1. Roger, I.; Shipman, M. A.; Symes, M. D., Earth-abundant catalysts for electrochemical and photoelectrochemical water splitting. *Nature Reviews Chemistry* **2017,** *1* (1), 1-13.
2. Huang, Z.-F.; Song, J.; Du, Y.; Xi, S.; Dou, S.; Nsanzimana, J. M. V.; Wang, C.; Xu, Z. J.; Wang, X., Chemical and structural origin of lattice oxygen oxidation in Co–Zn oxyhydroxide oxygen evolution electrocatalysts. *Nature Energy* **2019,** *4* (4), 329-338.
3. Cheng, W.; Zhao, X.; Su, H.; Tang, F.; Che, W.; Zhang, H.; Liu, Q., Lattice-strained metal–organic-framework arrays for bifunctional oxygen electrocatalysis. *Nature Energy* **2019,** *4* (2), 115-122.
4. Shan, J.; Guo, C.; Zhu, Y.; Chen, S.; Song, L.; Jaroniec, M.; Zheng, Y.; Qiao, S.-Z., Charge-redistribution-enhanced nanocrystalline Ru@ IrOx electrocatalysts for oxygen evolution in acidic media. *Chem* **2019,** *5* (2), 445-459.
5. Zhu, Y.; Tahini, H. A.; Hu, Z.; Chen, Z. G.; Zhou, W.; Komarek, A. C.; Lin, Q.; Lin, H. J.; Chen, C. T.; Zhong, Y., Boosting Oxygen Evolution Reaction by Creating Both Metal Ion and Lattice-Oxygen Active Sites in a Complex Oxide. *Advanced Materials* **2020,** *32* (1), 1905025.
6. Wang, A.; Li, J.; Zhang, T., Heterogeneous single-atom catalysis. *Nature Reviews Chemistry* **2018,** *2* (6), 65-81.
7. Chen, Y.; Ji, S.; Chen, C.; Peng, Q.; Wang, D.; Li, Y., Single-atom catalysts: synthetic strategies and electrochemical applications. *Joule* **2018,** *2* (7), 1242-1264.
8. Li, X.; Yang, X.; Huang, Y.; Zhang, T.; Liu, B., Supported Noble-Metal Single Atoms for Heterogeneous Catalysis. *Advanced Materials* **2019,** *31* (50), 1902031.
9. Lang, R.; Du, X.; Huang, Y.; Jiang, X.; Zhang, Q.; Guo, Y.; Liu, K.; Qiao, B.; Wang, A.; Zhang, T., Single-Atom Catalysts Based on the Metal–Oxide Interaction. *Chemical Reviews* **2020**.
10. Li, P.; Wang, M.; Duan, X.; Zheng, L.; Cheng, X.; Zhang, Y.; Kuang, Y.; Li, Y.; Ma, Q.; Feng, Z., Boosting oxygen evolution of single-atomic ruthenium through electronic coupling with cobalt-iron layered double hydroxides. *Nature communications* **2019,** *10* (1), 1-11.
11. Zhang, J.; Liu, J.; Xi, L.; Yu, Y.; Chen, N.; Sun, S.; Wang, W.; Lange, K. M.; Zhang, B., Single-atom Au/NiFe layered double hydroxide electrocatalyst: probing the origin of activity for oxygen evolution reaction. *Journal of the American Chemical Society* **2018,** *140* (11), 3876-3879.
12. Wang, Q.; Huang, X.; Zhao, Z. L.; Wang, M.; Xiang, B.; Li, J.; Feng, Z.; Xu, H.; Gu, M., Ultrahigh-loading of Ir single atoms on NiO matrix to dramatically enhance oxygen evolution reaction. *Journal of the American Chemical Society* **2020**.
13. Zhao, D.; Zhuang, Z.; Cao, X.; Zhang, C.; Peng, Q.; Chen, C.; Li, Y., Atomic site electrocatalysts for water splitting, oxygen reduction and selective oxidation. *Chemical Society Reviews* **2020,** *49* (7), 2215-2264.
14. Yang, Y.; Qian, Y.; Li, H.; Zhang, Z.; Mu, Y.; Do, D.; Zhou, B.; Dong, J.; Yan, W.; Qin, Y., O-coordinated W-Mo dual-atom catalyst for pH-universal electrocatalytic hydrogen evolution. *Science Advances* **2020,** *6* (23), eaba6586.
15. Su, D. W.; Ran, J.; Zhuang, Z. W.; Chen, C.; Qiao, S. Z.; Li, Y. D.; Wang, G. X., Atomically

dispersed Ni in cadmium-zinc sulfide quantum dots for high-performance visible-light photocatalytic hydrogen production. *Science advances* **2020,** *6* (33), eaaz8447.

16. Tang, C.; Zhang, R.; Lu, W.; Wang, Z.; Liu, D.; Hao, S.; Du, G.; Asiri, A. M.; Sun, X., Energy-saving electrolytic hydrogen generation: Ni2P nanoarray as a high-performance non-noble-metal Electrocatalyst. *Angewandte Chemie International Edition* **2017,** *56* (3), 842-846.
17. Chen, R.-S.; Huang, Y.-S.; Liang, Y.-M.; Tsai, D.-S.; Chi, Y.; Kai, J.-J., Growth control and characterization of vertically aligned IrO 2 nanorods. *Journal of Materials Chemistry* **2003,** *13* (10), 2525-2529.
18. Liu, P. F.; Li, X.; Yang, S.; Zu, M. Y.; Liu, P.; Zhang, B.; Zheng, L. R.; Zhao, H.; Yang, H. G., Ni2P (O)/Fe2P (O) interface can boost oxygen evolution electrocatalysis. *ACS Energy Letters* **2017,** *2* (10), 2257-2263.
19. Oyama, S. T.; Gott, T.; Asakura, K.; Takakusagi, S.; Miyazaki, K.; Koike, Y.; Bando, K. K., In situ FTIR and XANES studies of thiophene hydrodesulfurization on Ni2P/MCM-41. *Journal of Catalysis* **2009,** *268* (2), 209-222.
20. Seo, H.-R.; Cho, K.-S.; Lee, Y.-K., Formation mechanisms of Ni2P nanocrystals using XANES and EXAFS spectroscopy. *Materials Science and Engineering: B* **2011,** *176* (2), 132-140.
21. Sun, S.; Zhou, X.; Cong, B.; Hong, W.; Chen, G., Tailoring the d-Band Centers Endows (NixFe1–x)2P Nanosheets with Efficient Oxygen Evolution Catalysis. *ACS Catalysis* **2020**, 9086-9097.
22. Hansen, M. H.; Stern, L. A.; Feng, L.; Rossmeisl, J.; Hu, X., Widely available active sites on Ni2P for electrochemical hydrogen evolution--insights from first principles calculations. *Phys Chem Chem Phys* **2015,** *17* (16), 10823-9.
23. Norskov, J. K.; Rossmeisl, J.; Logadottir, A.; Lindqvist, L.; Kitchin, J. R.; Bligaard, T.; Jonsson, H., Origin of the overpotential for oxygen reduction at a fuel-cell cathode. *J Phys Chem B* **2004,** *108* (46), 17886-17892.
24. Rossmeisl, J.; Qu, Z. W.; Zhu, H.; Kroes, G. J.; Nørskov, J. K., Electrolysis of water on oxide surfaces. *Journal of Electroanalytical Chemistry* **2007,** *607* (1-2), 83-89.
25. Cai, C.; Han, S.; Wang, Q.; Gu, M., Direct Observation of Yolk–Shell Transforming to Gold Single Atoms and Clusters with Superior Oxygen Evolution Reaction Efficiency. *ACS Nano* **2019,** *13* (8), 8865-8871.